





 Cite this: *RSC Adv.*, 2019, 9, 5711

Synthesis and characterization of MgF_2 – CoF_2 binary fluorides. Influence of the treatment atmosphere and temperature on the structure and surface properties†

 Mariusz Pietrowski, * Michał Zieliński,  Emilia Alwin,  Agata Suchora and Joanna Gawarecka

Research was carried out on the incorporation of divalent cobalt cations into the crystalline structure of MgF_2 to form $\text{Mg}_x\text{Co}_{1-x}\text{F}_2$ binary fluorides, which had not been investigated before. The above fluorides were obtained by the precipitation from aqueous solution of magnesium and cobalt nitrates with ammonium fluoride. Binary fluorides containing 0.6, 7.5 and 37.7 mol% CoF_2 were prepared. The effects of treatment temperature (300, 400 °C) and atmosphere (oxidizing or reducing) on the structure (XRD, TPR- H_2 , UV-Vis), texture (low-temperature N_2 adsorption), surface composition (XPS) and surface acidity (NH_3 -TPD) of the binary fluorides were determined. It has been found that in $\text{Mg}_x\text{Co}_{1-x}\text{F}_2$ an isomorphic substitution occurs of Mg^{2+} cations by Co^{2+} cations which results in the formation of a rutile-type solid solution. The obtained binary fluorides are characterized by a mesoporous structure and relatively large surface area. It has been found that thermal treatment of the binary fluorides in oxidizing conditions results in the oxidation of CoF_2 to Co_3O_4 even at 300 °C; therefore it is not possible to obtain pure $\text{Mg}_x\text{Co}_{1-x}\text{F}_2$ binary fluorides in the presence of air. The preparation of the latter requires reducing conditions, namely thermal treatment of dry precipitate at 300 °C in an atmosphere of hydrogen. If the treatment is conducted at a higher temperature (400 °C), CoF_2 undergoes a partial reduction to metallic cobalt. An XPS study has shown the presence of hydroxyl groups in the investigated samples. However, these are solely surface groups because their presence was not detected by XRD measurements. The binary fluorides obtained by our method are characterized by a very narrow optical energy gap (5.31–3.50 eV), considerably narrower than that recorded for bulk fluorides. Measurements of temperature-programmed desorption of ammonia have shown that the incorporation of cobalt cations into the crystal structure of MgF_2 results in a decrease in the surface acidity of the binary fluorides.

 Received 13th November 2018
Accepted 6th February 2019

DOI: 10.1039/c8ra09365b

rsc.li/rsc-advances

1 Introduction

The commercial importance of inorganic fluorides is mainly a result of their application in metallurgy (rare-earth metals, aluminum, hafnium, zirconium), isotope separation and the manufacture of optical materials such as antireflective coatings. However, recently an increase has been observed in the interest in the application of inorganic fluorides in such areas as catalysis,^{1–7} photonics,^{8–10} biosensing,¹¹ reversible positive electrodes for rechargeable lithium batteries,^{12–18} high-temperature superconductor devices⁸ and supercapacitors.¹⁹ To tailor the properties of inorganic fluorides to the above applications, it is necessary to either use new ways of preparation^{15,16,20–27} or to

modify already known materials, among other things by isomorphic substitution of cations in the structure of a host with cations of a guest.^{28–34} This strategy has been adopted for the modification of catalytic properties of magnesium fluoride which has been applied since many years as a catalyst support.^{1,2,35–39} It is characterized by quite an inert surface which contains only Lewis acid centers of weak and moderate acid strength as well as weak basic sites.^{40,41} Kemnitz *et al.*⁴² adapted to mixed metal fluorides the Tanabe's model⁴³ explaining the Lewis acidity of the guest-host binary metal oxide systems. According to this model, isomorphic substitution of cations is possible, if sizes of host and guest cations are comparable. In the case when the positive charge of guest cation is greater than that of host cation, Lewis acidity is generated. By admixturing MgF_2 with transition metal ions at the oxidation state of +3 (Fe^{3+} , Cr^{3+} , V^{3+} , In^{3+} , Ga^{3+}), relatively strong Lewis acid sites are created.^{31,32,44–46} On the other hand, a change in the hydroxylation degree of high-surface area MgF_2 (HS- MgF_2) results in the

Adam Mickiewicz University in Poznań, Faculty of Chemistry, Umultowska 89B, 61-614 Poznań, Poland. E-mail: mariop@amu.edu.pl

† Electronic supplementary information (ESI) available. See DOI: 10.1039/c8ra09365b



formation of Brønsted acid centers, besides already mentioned Lewis acid sites, so the bi-acidic surface is obtained.^{47–49} The aforementioned modifications of MgF_2 concerned only the introduction of trivalent cations. No research was carried out on the modification of MgF_2 by divalent cations. Hence the idea to incorporate Co^{2+} cations into the crystal structure of MgF_2 . Cobalt(II) fluoride crystallizes in the rutile-type structure, as does magnesium fluoride, and ionic radii of both cations are comparable, therefore isomorphic substitution of Co^{2+} to replace Mg^{2+} and form a solid solution is perfectly possible.

In the past, an interest in the application of CoF_2 in practice was very small. Fu *et al.*⁵⁰ were the first who applied cobalt(II) fluoride as an anode in lithium ion batteries (LIBs). Not long after that, researchers began studying CoF_2 as a potential and promising anode candidate for LIBs.^{12,13,16–19,51–54}

Literature data on binary fluorides with bivalent cobalt are extremely scant. The only available data concern nickel–cobalt binary fluorides.^{12,19} However, there are no data on magnesium–cobalt binary fluorides. Teng *et al.*¹² obtained $\text{Ni}_x\text{Co}_{1-x}\text{F}_2$ binary fluorides and applied them in LIBs. During the precipitation of binary fluorides from a solution of cobalt and nickel nitrates with ammonium fluoride, they have used oleic acid as a surfactant. XRD analysis showed that Ni–Co binary fluorides have tetragonal structure (as do NiF_2 and CoF_2 alone) and the unit cell parameters decrease regularly with the increase in nickel content in the binary fluorides. Similar materials were obtained by Ding *et al.*,¹⁹ who used the solvothermal method and their starting compounds were nickel and cobalt acetates and hydrofluoric acid.

The research presented in this paper concerns the preparation of $\text{Mg}_x\text{Co}_{1-x}\text{F}_2$ binary fluorides with different Co content by a simple precipitation method and their detailed structural (XRD, TPR- H_2 , UV-Vis), textural (BET, BJH) and surface (XPS, NH_3 -TPD) characterizations as well as the determination of the effect of thermal treatment in reducing and oxidizing atmospheres on the structure. The replacement of Mg^{2+} ions by d-electron Co^{2+} ions should result in a change in electronic properties, thereby in a change of surface properties as well.

2 Experimental

2.1. Preparation of $\text{Mg}_x\text{Co}_{1-x}\text{F}_2$ binary fluorides

The binary fluorides were prepared by adding an aqueous solution of $\text{Mg}(\text{NO}_3)_2 \cdot 6\text{H}_2\text{O}$ and $\text{Co}(\text{NO}_3)_2 \cdot 6\text{H}_2\text{O}$ to an aqueous solution of NH_4F , followed by stirring with a magnetic stirrer for half an hour at room temperature. The formed precipitate was centrifuged and washed twice with distilled water. Then it was dried at 120 °C for 10 hours with temperature ramp of 0.1 °C min^{-1} . The dried samples were subjected to heating for 5 h at 300 and 400 °C (5 °C min^{-1} ramp) in oxidizing atmosphere (air, static conditions, electric resistance furnace) and reducing atmosphere (99.999% purity hydrogen flow; 50 ml min^{-1} , 5 °C min^{-1} ramp). The obtained samples with different cobalt content were denoted as MgCoX , where X stands for CoF_2 content expressed in mol% (taking the total content of $\text{MgF}_2 + \text{CoF}_2$ as 100%). For example, the sample consisting of 37.7 mol% CoF_2 and 62.3 mol% MgF_2 is denoted

as MgCo37.7 . For pristine MgF_2 the code is Mg100 , and for pristine CoF_2 it is Co100 . The composition of the samples and their codes are presented in Table 1. The samples heated in air were denoted as Ox, *e.g.* MgCo37.7-Ox , whereas those reduced with hydrogen were labeled R, *e.g.* MgCo37.7-R . Temperatures of the thermal treatment were denoted as 3 – for 300 °C and 4 – for 400 °C, *e.g.* MgCo37.7-Ox3 , MgCo37.7-R4 .

2.2. X-ray diffraction measurements (XRD)

The XRD measurements of the samples were carried out in the 2θ range from 5 to 80° on a powder diffractometer manufactured by PANalytical Ltd., using $\text{CuK}\alpha_1$ radiation. The unit cell parameters were calculated using WinPlotr and UnitCellWin software. The crystallite sizes of the samples were calculated by Scherrer's equation on the basis of the strongest 3–6 reflections.

2.3. X-ray photoelectron spectroscopy (XPS)

XPS spectra were obtained on a SPECS spectrometer equipped with non-monochromatic Al-K α source emitting photons of energy 1486.61 eV and a hemispherical analyzer (PHOIBOS 150 MCD NAP) set to pass energies of 60 eV and 20 eV for survey and regions, respectively. The XPS system base pressure was 1×10^{-9} mbar. The internal calibration of the XPS spectra was performed according to C–C binding energy value of 284.6 eV.

2.4. Scanning electron microscopy (SEM-EDS)

Scanning electron microscopy analysis was performed using a Quanta FEG 250 (FEI) microscope in high vacuum conditions at the acceleration voltage of 5 kV. The EDS analyses were conducted at beam acceleration voltage of 10 kV using an EDAX Octane SDD detector. To determine elemental compositions of samples, 9–15 EDS measurements were performed for 3–4 regions of each sample. The obtained results were averaged and measurement error was expressed as standard deviation.

2.5. UV-Vis spectroscopy

A UV-Vis spectrophotometer (Varian Cary 100) with an integrating sphere attachment for diffuse reflectance measurements was used to determine the optical band gap. The optical absorption was measured in the range of 200–1200 nm. The optical band-gap (E_g) was estimated using Kubelka–Munk function from variation of $(\alpha h\nu)^{1/2}$ with photon energy plots.

2.6. Temperature-programmed reduction (TPR- H_2)

Temperature-programmed reduction with hydrogen (TPR- H_2) was carried out by using an ASAP ChemiSorb 2705 instrument (Micromeritics). Catalyst samples of about 50 mg were reduced in a mixture of 10 vol% H_2 in Ar (99.999%, Linde) at a flow rate of 30 $\text{cm}^3 \text{min}^{-1}$ and a heating rate of 10 K min^{-1} . The hydrogen consumption was monitored with a thermal conductivity detector (TCD) and the signal intensity was normalized to 100 mg for each sample studied. The products of the reduction were retained by an isopropanol/liquid nitrogen cold trap at about –70 °C.



Table 1 The codes and composition of $\text{Mg}_x\text{Co}_{1-x}\text{F}_2$ binary fluorides as determined by EDS technique

Sample code	MgF_2 [mol%]	CoF_2 [mol%]	MgF_2 [wt%]	CoF_2 [wt%]	Standard deviation [wt%]
Mg100	100.0	0.0	100.0	0.0	0.5
MgCo0.6	99.4	0.6	99.1	0.9	0.6
MgCo7.5	82.5	7.5	88.9	11.1	0.9
MgCo37.7	62.3	37.7	51.8	48.2	0.6
Co100	0.0	100.0	0.0	100	0.5

2.7. BET surface area and porosity measurements

The Brunauer–Emmett–Teller surface areas were determined by nitrogen adsorption at -196°C using a Micromeritics ASAP 2010 sorptometer. The total pore volumes and average pore diameters were determined by applying the Barrett–Joyner–Halenda (BJH) method to the isotherm desorption branch.

2.8. Temperature-programmed desorption of NH_3 (NH_3 -TPD)

The temperature-programmed desorption of NH_3 (NH_3 -TPD) was carried out using an ASAP ChemiSorb 2705 instrument (Micromeritics). Catalyst samples of about 500 mg were activated *in situ* for 1 h at 300°C in helium at a flow rate of $30\text{ cm}^3\text{ min}^{-1}$. Then they were cooled down to 100°C and contacted with NH_3 for 10 min at a flow rate of $10\text{ cm}^3\text{ min}^{-1}$ followed by flushing with helium for 30 min. Measurements of temperature-programmed desorption were conducted in helium flow ($30\text{ cm}^3\text{ min}^{-1}$) at a heating rate of 10 K min^{-1} . The desorbing ammonia was monitored with a thermal conductivity detector (TCD) and the signal intensity was normalized to 1 g for each sample studied. The calibration was performed by dispensing $1\text{ cm}^3\text{ NH}_3$ from a calibrated gas loop into the helium flow.

3.2. X-ray powder diffraction measurements – phase composition of binary fluorides

Fig. 1a shows XRD patterns of samples reduced at 300°C . The location and intensity of reflections originating from Mg100 sample corresponds to the data contained in the PDF database for magnesium fluoride (sellaite, PDF 41-1443). No significant changes were observed in the position of reflections for MgCo0.6-R3 sample. At a greater Co content (the samples MgCo7.5-R3 and MgCo37.7-R3), the reflections became shifted towards smaller 2θ angles which indicates the replacement of Mg^{2+} ions by Co^{2+} ions. The shift of reflections towards smaller angles is indicative of an increase in experimental lattice parameters as the cobalt content is increased in the solid solution. The increase in the lattice parameters with increased cobalt content is due to the larger ionic radius of Co^{2+} compared to that of Mg^{2+} (0.735 and 0.72 \AA , respectively⁵⁵). Simultaneously, a decrease in intensities of the reflections occurs, which is particularly clear in the case of the MgCo37.7-R3 sample, *i.e.* it indicates a decline in the sample crystallinity. In Fig. 1b X-ray diffraction patterns are presented of samples reduced at 400°C . Higher reduction temperature resulted in sharper reflections which became narrower and more intense and this points to a better crystallinity of the obtained samples. However, trace amounts of metallic cobalt (PDF 5-727) have been observed after reduction at 400°C (it concerns Co100-R4 and MgCo37.7-R4 samples).

3 Results and discussion

3.1. Visual analysis of the samples

The obtained gel-like precipitates of $\text{Mg}_x\text{Co}_{1-x}\text{F}_2$ binary fluorides were subjected to drying at 120°C followed by grinding to powder in an agate mortar. Pictures of the samples are shown in Table S1 in ESI†. Pristine magnesium fluoride was white, whereas pristine cobalt(II) fluoride was pink-colored. On the other hand, binary fluorides assumed different hues of pink with the intensity increasing with the rise in CoF_2 content.

The dry samples were heated at 300 and 400°C in either reducing (hydrogen) or oxidizing (air) atmosphere. Pristine MgF_2 remained white irrespective of the kind of atmosphere and heating temperature. After the thermal treatment at 300 and 400°C in air, the samples containing 7.5 and $37.7\text{ mol}\%$ CoF_2 changed their color to almost black which can indicate oxidation to cobalt oxides. On the other hand, after heating at 300°C in hydrogen, no clear change in color was observed which suggests the preservation of the structure of binary fluorides with no admixture of other phases.

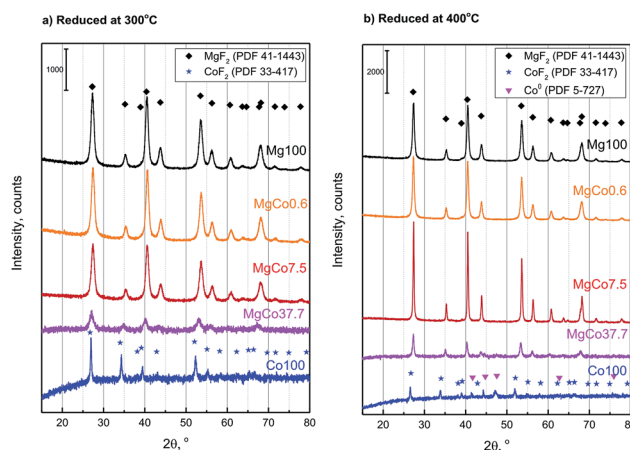


Fig. 1 Powder diffraction patterns of $\text{Mg}_x\text{Co}_{1-x}\text{F}_2$ binary fluorides reduced for 5 h with pure hydrogen at 300°C (a) and 400°C (b).



Pristine MgF_2 is oxygen-resistant at high temperatures and no presence of oxide phase (MgO) was detected even after calcination at 500°C . CoF_2 , unlike MgF_2 , undergoes during the calcination a gradual transformation into oxofluorides and then into oxides as proved by XRD studies of samples calcined at 300 and 400°C (ESI – Fig. S1†). That is why it was impossible to obtain pure-phase bifluorides during the treatment in oxidizing atmosphere.

The unit cell parameters of the samples reduced at 300 and 400°C were determined using programs WinPlotr and UnitCellWin. According to different sources, the unit cell parameter a of MgF_2 ranges from 4.621 to 4.628 \AA and c parameter from 3.0159 to 3.0534 \AA .^{56–58} Analogously, for CoF_2 a (4.6950 – 4.6956) and c (3.1774 – 3.1817)^{57,59,60} (Table S2†). Similarly, the c/a ratio changes in the range 0.6526 – 0.6606 for MgF_2 and 0.6767 – 0.6777 for CoF_2 . Changes in the composition of investigated samples are accompanied by changes in the unit cell parameters (Fig. 2). It should be mentioned that these changes are not regular. Initially, a slight decrease in a and c parameters occurs with increasing Co content (MgCo0.6 and MgCo7.5 samples), however, only the incorporation of 37.7 mol\% Co causes a significant increase of the above parameters. Crystallite sizes estimated on the basis of Scherrer's formula for Mg100-R3 , MgCo0.6-R3 and MgCo7.5-R3 samples are of about 10 nm , whereas for MgCo37.7-R3 only 8 nm . No magnesium-containing sample, that is characterized by the narrowest reflection, contains crystallites of about 25 nm in size. The poor crystallinity of the MgCo37.7-R3 sample and large accumulation of defects can be an asset from the viewpoint of catalysis, because defects are often adsorption centers for reaction substrates and during the preparation of catalysts they play the role of adsorption sites for active phase. The aforementioned large amorphicity has also been reflected in high specific surface area of the above sample (see next subsection). Of course, an increase in the thermal treatment temperature leads to a rise in crystallite size.

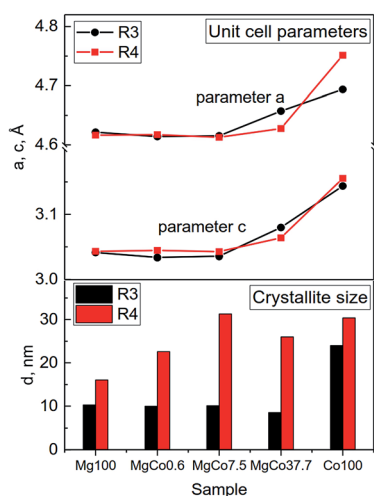


Fig. 2 Changes in unit cell parameters (a and c) and crystallite sizes d for $\text{Mg}_x\text{Co}_{1-x}\text{F}_2$ binary fluorides reduced at 300 and 400°C .

Summing up, XRD measurements point to a possibility of obtaining $\text{Mg}_x\text{Co}_{1-x}\text{F}_2$ binary fluorides with rutile-type structure. The fact that no separate MgF_2 and CoF_2 phases have been found in the binary fluoride samples proves the formation of rutile-type structure in which Mg^{2+} and Co^{2+} ions are homogeneously dispersed and occupy the same lattice positions. However, it has to be emphasized that the preparation of high purity $\text{Mg}_x\text{Co}_{1-x}\text{F}_2$ binary fluoride systems requires using oxygen-free atmosphere (preferably reducing one) and relatively low temperature of about 300°C (Table 2).

The application of a higher temperature causes the separation of metallic cobalt phase, whereas the application of oxidizing atmosphere leads to the formation of Co_3O_4 .

3.3. Temperature-programmed reduction (TPR- H_2)

The measurements of temperature-programmed reduction with hydrogen (TPR- H_2) provide information about reducibility of chemical compounds present in a sample and about their interactions, thus enabling to draw conclusions on the phase composition of a sample. The TPR- H_2 measurements can confirm the presence of solid solution in the bifluoride samples. However, this should be preceded by the determination of reduction temperatures of cobalt ions present in the form of oxide and fluoride. To this end, TPR- H_2 measurements of reduced and oxidized samples were carried out.

According to literature data,^{61–63} the reduction of Co_3O_4 proceeds in two stages:



Fig. 3 shows TPR- H_2 profiles of Co100 and MgCo37.7 samples heated in air at 300 and 400°C . The two-stage reduction finds reflection in the shape of TPR- H_2 profile of the Co100-Ox4 sample as two peaks at 355 and 398°C .⁶¹ The shape of TPR- H_2 curve of Co_3O_4 is very distinctive and was observed many times,^{61,63–66} including the $\text{Co}_3\text{O}_4/\text{MgF}_2$ system.⁶⁷ Therefore, the small signal at 457°C should be ascribed to the reduction of CoF_2 . Similar signals are also visible in the TPR- H_2 profile of the Co100-Ox3 sample subjected to oxidation at 300°C . The presence of a small amount of cobalt oxide is indicated by the signal in the temperature range of 300 – 440°C . Above this temperature, the reduction of CoF_2 occurs. In Fig. 3b presented are TPR- H_2 profiles of the MgCo37.7-Ox sample after its oxidation at 300 and 400°C . As it was in the case of pristine CoF_2 sample, the calcination at 400°C results in the appearance of signals originating from the reduction of cobalt oxide (300 – 440°C) and the reduction of CoF_2 (550 – 570°C). However, worth noting is the fact that the reduction of CoF_2 in the binary fluorides proceeds at a considerably higher temperature than in the case of the Co100 sample. We believe that this is a result of a stabilization of CoF_2 in the matrix formed by MgF_2 .

The TPR- H_2 profiles of the MgCo7.5-Ox sample (not shown) have also indicated the presence of analogous signals, however, their intensity was several times smaller. No signals were observed in the case of Mg100-Ox and MgCo0.6-Ox samples,



Table 2 Phase identification on the basis of XRD results

Sample	Reduced		Oxidized	
	300 °C	400 °C	300 °C	400 °C
Mg100	MgF ₂	MgF ₂	MgF ₂	MgF ₂
MgCo0.6	MgF ₂	MgF ₂	MgF ₂	MgF ₂
MgCo7.5	Mg _x Co _{1-x} F ₂	Mg _x Co _{1-x} F ₂ + Co ⁰	Mg _x Co _{1-x} F ₂ + Co ₃ O ₄	Mg _x Co _{1-x} F ₂ + Co ₃ O ₄
MgCo37.7	Mg _x Co _{1-x} F ₂	Mg _x Co _{1-x} F ₂ + Co ⁰	Mg _x Co _{1-x} F ₂ + Co ₃ O ₄	Mg _x Co _{1-x} F ₂ + Co ₃ O ₄
Co100	CoF ₂	CoF ₂ + Co ⁰	CoF ₂ + Co ₃ O ₄	Co ₃ O ₄

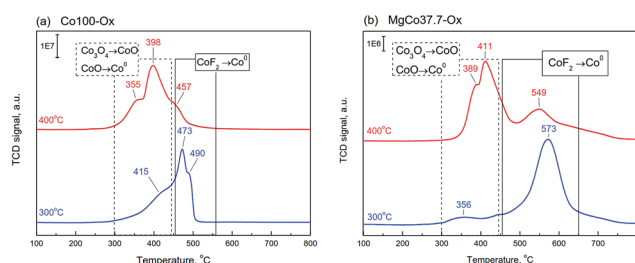


Fig. 3 TPR-H₂ profiles of the samples Co100-Ox (a) and MgCo37.7-Ox (b), calcined at 300 and 400 °C (signal intensity was normalized to 100 mg).

which is not surprising because magnesium fluoride is highly resistant to reduction.

The method of synthesis applied by us consists in adding magnesium and cobalt nitrates to a solution of ammonium fluoride which yields ammonium nitrate and a precipitate of binary fluorides. The obtained precipitate was thoroughly washed to remove NH₄NO₃ and TPR measurements show that the removal was complete. According to literature data,^{68–70} the thermal decomposition of ammonium nitrate proceeds in the range of 200–300 °C. In the TPR profiles of our binary fluorides no signals associated with the decomposition of NH₄NO₃ were detected, which proves high purity of the obtained materials.

To observe the reduction of CoF₂ we have conducted TPR-H₂ measurements of Co100, MgCo37.7 and MgCo7.5 samples heated in hydrogen at 300 °C (Fig. 4). Pristine cobalt fluoride

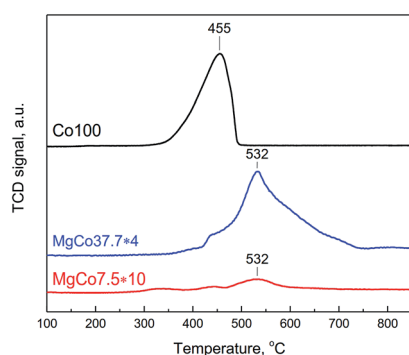


Fig. 4 TPR-H₂ profiles of Co100-R3, MgCo37.7-R3 and MgCo7.5-R3 samples (signal intensity was normalized to 100 mg and signal intensities for MgCo37.7-R3 and MgCo7.5-R3 were multiplied by 4, and 10, respectively).

(Co100-R3) undergoes reduction at 455 °C, whereas CoF₂ dispersed in the MgF₂ matrix (MgCo37.7 and MgCo7.5) shows considerably higher thermal stability – the peak maximum occurs at a significantly higher temperature (532 °C). Moreover, the shape of the profiles is different – in the case of Co100-R3 it is narrower and the reduction is completed around 500 °C, whereas in that of MgCo37.7-R3 the profile is very broad and the reduction lasts to almost 750 °C. We believe that such a large shift in the reduction temperature of CoF₂ is a result of the stabilization of Co²⁺ ions in the binary fluoride structure due to the neighborhood with Mg²⁺ ions, which increases the resistance to reduction.

3.4. Textural analysis of the samples

Results presented so far clearly show that obtaining mono-phasic binary fluorides is possible only by thermal treatment in reducing conditions at a temperature not exceeding 300 °C. In oxidizing conditions, cobalt oxide phase is formed in addition to fluoride phase, whereas reduction at 400 °C results in the formation of metallic cobalt phase. Hence textural studies were performed for the samples reduced at 300 °C.

Specific surface area and porous structure of the samples were determined from low-temperature nitrogen adsorption/desorption isotherms. Results of the measurements are presented in Table 3 and Fig. 5.

Specific surface area of reduced samples ranges from 16.0 to 49.0 m² g^{−1}. With increasing cobalt content in the samples of binary fluorides, a regular rise in surface areas was observed. The highest surface area (49.0 m² g^{−1}) was found for the MgCo37.7 sample. Simultaneously, a decrease in average pore diameter from 8.0 to 3.9 nm and in cumulative pore volume from 0.132 to 0.095 cm³ g^{−1} was observed (Table 3, Fig. 5). Only the sample Co100 has a considerably smaller surface area (16.0

Table 3 Textural analysis of samples reduced at 300 °C

Sample	Textural parameter		
	BET surface area, m ² g ^{−1}	Average pore diameter, nm	Cumulative pore volume, cm ³ g ^{−1}
Mg100	36.5(1)	8.0	0.132
MgCo0.6	40.9(1)	5.9	0.116
MgCo7.5	42.7(1)	6.6	0.117
MgCo37.7	49.0(2)	3.9	0.096
Co100	16.0(1)	27.2	0.095



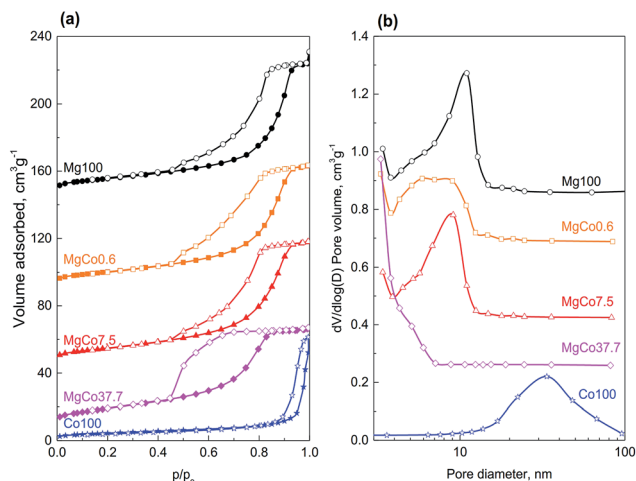


Fig. 5 Nitrogen physisorption isotherms (a) and pore volume distribution as a function of pore diameter (b) for the samples heated in hydrogen at 300 °C. The curves are shifted along Y axis for clarity.

$\text{m}^2 \text{g}^{-1}$) which is a result of the presence of much greater pores (27.2 nm).

All isotherms recorded for the studied samples belong to the type IV(a) according to the IUPAC classification,⁷¹ *i.e.* the type that is characteristic of mesoporous materials. The isotherms measured for the samples Mg100, MgCo0.6 and MgCo7.5, are similar one to another – their hysteresis loops start at relative pressures p/p_0 of about 0.4 and belong to the type H2(b). Such a shape of hysteresis loop is characteristic of mesoporous adsorbents containing ink-bottle shaped pores with varied neck sizes. Somewhat different shape of hysteresis loop occurs in the case of the MgCo37.7 sample. It is characterized by a steep desorption branch, which is a characteristic feature of H2(a) loops, and can be attributed to either pore-blocking/percolation in a narrow range of pore necks or to cavitation-induced evaporation. The average pore size calculated by the BJH method on the basis of the isotherm desorption branch is 3.9 nm. However, this result (and also the pore size distribution curve – Fig. 5b) should be considered as an approximation only and not an accurate assessment, because in the case of the MgCo37.7 sample we most likely deal with cavitation-controlled evaporation, and in such a situation no quantitative information about the neck size and neck size distribution can be obtained.⁷¹ The Co100 sample, *i.e.* pristine cobalt fluoride heated in hydrogen at 300 °C, has considerably smaller surface area ($16.0 \text{ m}^2 \text{g}^{-1}$) compared to the binary fluorides. The nitrogen physisorption isotherm remains of type IV(a), however, the hysteresis loop of type H1 indicates the presence of wide mesopores.

3.5. Band gap estimation

For the samples reduced at 300 °C, for which the presence was confirmed of monophasic binary fluorides $\text{Mg}_x\text{Co}_{1-x}\text{F}_2$, the optical band-gap energy (Table 4) was determined by the Kubelka–Munk method on the basis of UV-Vis reflectance spectra. The value obtained for pristine MgF_2 was 5.31 eV. It was decreasing with increasing cobalt content, to reach 3.50 eV for

Table 4 The optical band gap estimated using Kubelka–Munk function from variation of $(\alpha h\nu)^{1/2}$ with photon energy plots

Sample	Band gap, eV
Mg100	5.31
MgCo0.6	5.40
MgCo7.5	5.22
MgCo37.7	4.85
Co100	3.50

pristine CoF_2 . The value of 5.31 eV obtained for pristine MgF_2 seems to be significantly underestimated when confronted with literature data, according to which it is ~ 10.8 eV (ref. 72) for bulk MgF_2 . However, for MgF_2 in the form of thin films, the value of energy gap is 3.8 eV,⁷³ whereas theoretical calculations give the value of 5.95 eV (ref. 72) or 6.83 eV.⁷⁴ In the light of the above data the obtained by us value of 5.31 eV may be real. It is worth mentioning that MgF_2 obtained in our study can hardly be called “bulk”, because XRD and porosity measurements showed that it is a mesoporous fine-crystalline material with crystallites as small as 10 nm.

3.6. XPS spectroscopy

Information obtained from XRD and TPR- H_2 measurements concerned bulk structure of binary fluorides. They showed that $\text{Mg}_x\text{Co}_{1-x}\text{F}_2$ binary fluorides have rutile-type structure and that high-temperature treatment (400 °C) in reducing conditions results in a partial reduction of cobalt cations to metallic cobalt, whereas in oxidizing conditions to the formation of some amount of Co_3O_4 . These results should find confirmation by XPS measurements, albeit the latter provide information on surface elemental composition, because the depth of XPS analysis is of a few nanometers.

The survey XPS spectra of MgF_2 , CoF_2 and $\text{Mg}_x\text{Co}_{1-x}\text{F}_2$ binary fluorides are presented in Fig. S2.† In addition to the lines of main elements: fluorine, magnesium and cobalt, also carbon and oxygen were detected in the measurements.

Fig. 6a shows high-resolution XPS spectra of Mg 2p for $\text{Mg}_x\text{Co}_{1-x}\text{F}_2$ binary fluorides and pristine MgF_2 . For all the samples a single broad signal was detected in the range of 50.4–51.2 eV, which most likely can be ascribed to Mg^{2+} in MgF_2 . In the case of pristine MgF_2 , the signal occurs at 51.2 eV. The addition of cobalt results in a decrease of binding energy to 50.7–51.0 eV for MgCo37.7-R4 and both oxidized samples (MgCo37.7-Ox3 and MgCo37.7-Ox4), whereas in the case of the sample MgCo37.7-R4 to 50.4 eV. Various studies^{75–79} have shown that the position of the Mg 2p line provides no possibility to discriminate between magnesium in the form of oxide, hydroxide or fluoride. In our samples the fluoride is obviously the most likely form, however, it does not rule out a possibility of a coexistence of magnesium in the form of hydroxide or oxide. Fig. 6b shows XPS spectra of O 1s. A signal at binding energy (BE) of 531.0–532.5 eV has been observed for the samples heated at 300 °C (both binary fluorides and pristine MgF_2). The signal can be ascribed neither to MgO for which O 1s binding



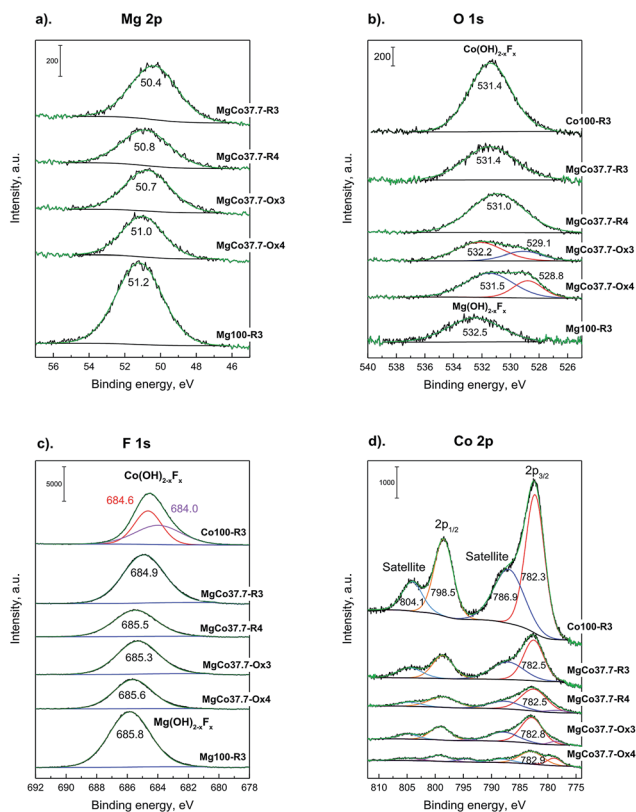


Fig. 6 XPS spectra of Mg 2p (a), O 1s (b), F 1s (c), Co 2p (d) photoemission line for $\text{Mg}_x\text{Co}_{1-x}\text{F}_2$ binary fluorides.

energy is about 531 eV nor to $\text{Mg}(\text{OH})_2$ for which BE is 533.2 eV.^{75,76,78,80–82} A more likely interpretation can be made by analyzing the difference in O 1s – Mg 2p chemical shift. In the case of MgO the difference is by about 1.3 eV smaller than in that of $\text{Mg}(\text{OH})_2$. In Table 5, listed are chemical shifts and differences in the shifts (ΔE) for the studied binary fluorides, MgF_2 and CoF_2 .

The analysis indicates the presence of hydroxyl groups on surfaces of binary fluorides and pristine MgF_2 heated at 300 °C (irrespective of treatment atmosphere) which is proved by ΔE O 1s – Mg 2p values of 481.0–481.5 eV (ref. 79 and 83) and by many

earlier reports on hydroxylated MgF_2 .^{1,35,36,40,47–49,84–87} Verdier *et al.*^{79,83} ascribed them to the $\text{Mg}(\text{OH})_{2-x}\text{F}_x$ species. The presence of surface complexes of such a type is indicated by the values of ΔE F 1s – Mg 2p that are equal to 634.5–634.7 eV, which in the case of crystalline MgF_2 are about 633 eV and in that of $\text{Mg}(\text{OH})_{2-x}\text{F}_x$ they range between 634.5 and 635.0 eV.⁷⁹ After reduction at 400 °C, the O 1s peak undergoes a shift towards lower energies (531.0 eV), which results in a decrease in the O 1s – Mg 2p difference to 480.2 eV and the latter value is characteristic of MgO .^{79,83} A similar situation was observed when oxidation was carried out at 400 °C. The appearance of the O 1s peak in the position corresponding to MgO results from the fact that the MgF_2 surface undergoes dehydroxylation during heating at higher temperatures, according to the equation $\text{OH}^- + \text{OH}^- \rightarrow \text{H}_2\text{O} + \text{O}^{2-}$. The above reaction leads to the gradual decay of hydroxyl groups and the appearance of O^{2-} anions in place of them. The binary fluorides subjected to heating in the oxidizing atmosphere react in a similar way. After oxidation at 300 °C, the O 1s signal (Fig. 6b) appears at BE of 532.2 eV, which points to the presence of surface complexes of $\text{Mg}(\text{OH})_{2-x}\text{F}_x$ type, and after oxidation at 400 °C it undergoes a shift to 531.5 eV, *i.e.* the position characteristic of MgO .⁸⁸ Moreover, a new signal around 529 eV appears in the spectra of calcined samples that can be ascribed to Co_3O_4 .^{16,89–93} In the case of O 1s photoelectrons of pristine CoF_2 subjected to reduction at 300 °C (Co100-R3 – Fig. 6b), the peak occurs at 531.4 eV. This signal cannot be attributed to cobalt oxide because in the case of the latter the discussed signal occurs around 529–530 eV.^{91,92} In this situation it would be justified to assume the interpretation analogous to that for MgF_2 , *i.e.* to ascribe the O 1s signal at 531.4 eV to the complex of $\text{Co}(\text{OH})_{2-x}\text{F}_x$ type.¹⁶ This means that the surface of CoF_2 , similarly to that of MgF_2 , when exposed to water vapor-containing environment, adsorbs water molecules that form surface OH groups. The XPS spectrum for F 1s is presented in Fig. 6c. For pristine MgF_2 and all binary fluorides one broad peak with maximum in the range 685.8–684.9 eV has been observed, irrespective of the composition of binary fluorides, treatment temperature and atmosphere. The mentioned signal originates from fluorine bound in the complex of $\text{Mg}(\text{OH})_{2-x}\text{F}_x$ type. This is indicated both by the BE value itself and the difference ΔE F 1s – Mg 2p (Table 5). The binding energy

Table 5 Chemical shifts and differences (ΔE) in chemical shifts for $\text{Mg}_x\text{Co}_{1-x}\text{F}_2$ binary fluorides, MgF_2 and CoF_2

Sample	Binding energy (eV)			ΔE (eV)			
	Mg 2p	F 1s	O 1s	O 1s – Mg 2p	Assignment	F 1s – Mg 2p	Assignment
Mg100-R3	51.2	685.8	532.5	481.3	Mg–OH	634.6	$\text{Mg}(\text{OH})_{2-x}\text{F}_x$
MgCo37.7-R3	50.4	684.9	531.4	481.0	Mg–OH	634.5	$\text{Mg}(\text{OH})_{2-x}\text{F}_x$
MgCo37.7-R4	50.8	685.5	531.0	480.2	Mg–O	634.7	$\text{Mg}(\text{OH})_{2-x}\text{F}_x$
MgCo37.7-Ox3	50.7	685.3	532.2	481.5	Mg–OH	634.6	$\text{Mg}(\text{OH})_{2-x}\text{F}_x$
MgCo37.7-Ox4	51.0	685.6	529.1	480.5	Mg–O	634.6	
			528.8				
Co100-R3	—	684.6 684.0	531.4	—	—	—	$\text{Mg}(\text{OH})_{2-x}\text{F}_x$



difference from the fluorine core level and magnesium (ΔE F 1s – Mg 2p) is ~ 634.6 eV. As already mentioned, according to Verdier *et al.*,⁷⁹ this difference for MgF_2 should be 632.9 eV.

The value observed in the case of our samples is larger and can be ascribed to $\text{Mg}(\text{OH})_{2-x}\text{F}_x$ – type magnesium hydroxyfluoride.⁹⁴

Similarly, for pristine CoF_2 a signal at 684.6 eV was observed, which by analogy to MgF_2 can be attributed to complexes of $\text{Co}(\text{OH})_{2-x}\text{F}_x$ type. The Co 2p core level spectrum is characterized by two components appearing due to spin-orbital splitting Co 2p_{3/2} and Co 2p_{1/2}, and shake-up satellites (Fig. 6d and 7). The high spin Co^{2+} compounds such as CoO, $\text{Co}(\text{OH})_2$ and CoF_2 exhibit strong satellite lines which are located at about 5–6 eV above the photo line.^{54,89,95,96} The main Co 2p_{3/2} peak for Co^{2+} in compounds such as CoO and $\text{Co}(\text{OH})_2$ usually occurs around 780–781 eV.^{63,91,95} In the case of CoF_2 , it is shifted towards higher energies and occurs at about 783 eV as reported in ref. 17 and 54. All the recorded spectra have such a complex structure. The Co 2p_{3/2} feature around 783 eV and the intense shake-up satellite peak at 788 eV are visible in the obtained XPS spectra and originate from Co^{2+} in CoF_2 .^{17,54,96} Spin-orbital splitting between the Co 2p_{3/2} and Co 2p_{1/2} is at about 16 eV (Table 6) and is characteristic of Co^{2+} .^{95,97} An additional signal at 778.5 eV appeared in the spectrum of the sample reduced at 400 °C. This feature can be unambiguously assigned to metallic cobalt.⁸⁹ Such a conclusion is in agreement with results of XRD measurements which showed the presence of metallic cobalt in the MgCo37.7-R4 sample.

In the spectra of oxidized samples, the Co^{3+} 2p_{3/2} (at about 778.9 eV) and Co 2p_{1/2} (at about 794.4 eV) signals, attributed to Co^{3+} ions,⁶³ are visible at lower BE values. In contradistinction to the high spin Co^{2+} compounds, the low spin Co^{3+}

compounds, such as Co_3O_4 , are characterized by a very weak satellite.^{91,95} In the case of our samples, due to the presence of intense signals from Co^{2+} in CoF_2 , satellite bands from Co^{3+} are practically invisible. The results of the XPS study are fully consistent with the results of XRD and TPR- H_2 measurements which pointed to the presence of the Co_3O_4 phase in the calcined samples.

The XPS results prove that on surfaces of the binary fluorides (as well as Mg and Co fluorides alone) present are hydroxyl groups as indicated by the positions of F 1s and O 1s signals. The question arises why did not the presence of OH groups affect the crystalline structure of the binary fluorides? It can be a result of the fact that the effective ionic radii of F^- and OH^- do not differ much – the OH^- ion is only slightly greater than F^- ion (by about 0.3 nm (ref. 98)), hence any changes in the unit cell parameters caused by the replacement of F^- by OH^- would be slight. However, they should be noticeable because the introduction of OH^- groups into the MgF_2 structure results in a small increase in the lattice constant a and a decrease in the c constant, as proved by Booster *et al.*⁸⁴ We have not observed such changes, hence our conclusion is that the proposed $\text{Mg}(\text{OH})_{2-x}\text{F}_x$ groups are the only surface complexes. A conclusion that similar complexes are present on the surface of CoF_2 seems to be interesting. The XPS measurements have shown that in the case of CoF_2 we deal with the phenomenon analogous to that of MgF_2 , *i.e.* the surface fluoride ions are replaced by hydroxyl groups. Such a phenomenon was not reported yet.

3.7. Surface acidity characterization by NH_3 -TPD measurements

The studies carried out by Kemnitz *et al.*^{31,32,42,44,46} have shown that the substitution of divalent cation with trivalent cation in the structure of MgF_2 results in an increase in Lewis acidity of binary fluorides, as predicted by the Tanabe's model.⁴³ The aforementioned model does not predict a rise in the acidity as a result of the substitution of cations with the same valence, hence in the case of the incorporation of Co^{2+} cation into the MgF_2 lattice, no increase in the acidity should be expected. However, such an incorporation will modify electronic properties of the binary fluoride, because the presence of d orbitals in cobalt atom should affect charge distribution in the lattice of the binary fluoride, which play the role of Lewis acid centers. A certain diffusion of the charge, particularly as concerns the positive charge localized on cations, can be expected which will result in a reduction in Lewis acidity of binary systems.

The above hypothesis was verified by determining the concentration of acid sites on the surface of binary fluorides using the NH_3 -TPD technique (Fig. 8). The measurements were conducted for the samples reduced at 300 °C. The shape of NH_3 -TPD profiles indicates that the acid centers differ in their strength which is clearly visible as a distinct inflection in the TPD curves. The concentration of acid centers on surfaces of the Mg100-R3 and MgCo0.6-R3 samples was almost the same. Hence, one can conclude that the incorporation of 0.6 mol% CoF_2 into the structure of MgF_2 has a negligible effect on the acid properties. A distinct change appears only for MgCo7.5-R3

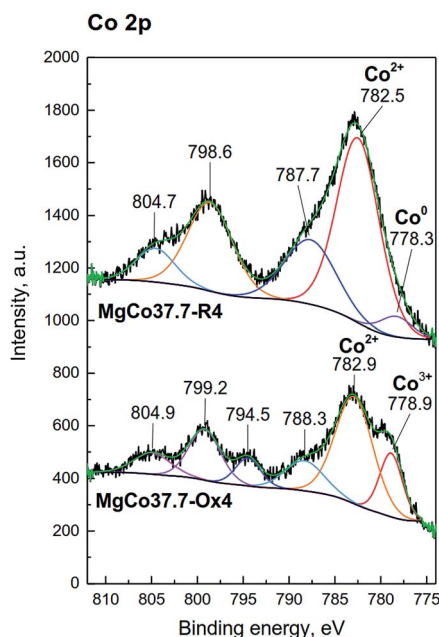
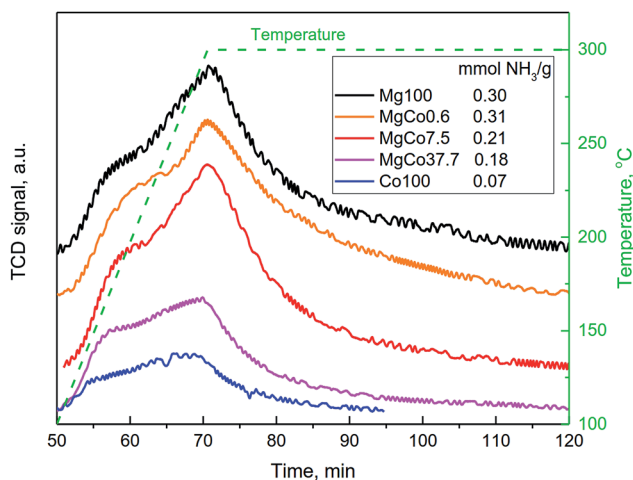


Fig. 7 XPS spectra of the Co 2p photoemission line for MgCo37.7 samples reduced and oxidized at 400 °C.



Table 6 Binding energies, orbital splitting and differences in binding energies for binary fluorides

Sample	Binding Energy (eV)				Orbital splitting		ΔE Satellite-2p _{3/2}
	Co 2p _{3/2}	Satellite	Co 2p _{1/2}	Satellite	2p _{1/2} -2p _{3/2}		
Co100-R3	—	782.3	786.9	—	798.5	804.1	4.6
MgCo37.7-R3	—	782.5	787.1	—	798.6	804.5	4.6
MgCo37.7-R4	778.3	782.5	787.7	—	798.6	804.6	5.2
MgCo37.7-Ox3	778.6	782.8	787.9	794.4	799.1	804.9	5.1
MgCo37.7-Ox4	778.9	782.9	788.3	794.5	799.2	804.9	5.4

Fig. 8 NH₃-TPD profiles of Mg_xCo_{1-x}F₂ binary fluorides after reduction at 300 °C.

and MgCo37.7-R3 samples, where the concentration of acid centers falls from the initial $\sim 0.3 \text{ mmol g}^{-1}$ to 0.21 and 0.18 mmol g^{-1} , respectively. The lowest acidity (0.07 mmol g^{-1}) was found for pristine CoF₂.

Summing up, the NH₃-TPD measurements have shown that the substitution of Mg²⁺ ions with Co²⁺ ions in the structure of MgF₂ leads to a decrease in the surface acidity which is probably caused by the presence of d orbitals in cobalt atoms and diffusion of the positive charge localized on surface cations being Lewis acid sites.

4 Conclusions

New binary fluoride systems consisting of magnesium fluoride doped with cobalt fluoride were synthesized and characterized in detail. The Mg_xCo_{1-x}F₂ binary fluorides with cobalt content from 0.6 to 37.7 mol% (1–50 wt%) were obtained for the first time by applying a simple method consisting in the precipitation from aqueous solutions of magnesium and cobalt nitrates with ammonium fluoride solution. All the obtained materials have tetragonal rutile-type structure (*P4₂/mnm*) in which the cationic positions of magnesium were isomorphically substituted by cobalt ions. The unit cell parameters (*a* and *c*) determined on the basis of XRD measurements increase with increasing cobalt content in the Mg_xCo_{1-x}F₂ binary fluorides

and assume intermediate values between those characteristic of MgF₂ and CoF₂. As the CoF₂ content in the binary fluorides rises, the degree of disorder of the structure increases which results in an increase in the porosity and surface area. The sample containing 37.7 mol% of CoF₂, subjected to the reduction at 300 °C, was characterized by the largest surface area. It has been established that the preparation of pure phase of Mg_xCo_{1-x}F₂ binary fluorides requires reducing atmosphere during the thermal treatment, the temperature of which should not exceed 300 °C. At higher temperatures the separation of metallic cobalt phase occurs and in the case of oxidizing conditions, Co₃O₄ is formed. The presence of cobalt oxides in the calcined samples and the formation of metallic cobalt in the samples reduced at 400 °C has been confirmed by three independent techniques: XRD, TPR-H₂ and XPS. An interesting fact is the detection of hydroxyl groups not only on the surfaces of pristine MgF₂ and binary fluorides, but also on the surface of CoF₂. High intensity of the O 1s peak in the XPS spectrum of pristine CoF₂ indicates that the concentration of hydroxyl groups on its surface is even greater than on the surface of MgF₂. Surface complexes of magnesium and cobalt hydroxyfluorides can be described by the following molecular formulae: Mg(OH)_{2-x}F_x and Co(OH)_{2-x}F_x. The UV-Vis measurements have shown that both binary fluorides and pristine fluorides (MgF₂ and CoF₂) are characterized by narrow optical energy gap (5.31–3.50 eV), considerably narrower than those recorded for bulk fluorides. The NH₃-TPD measurements have shown that the substitution of Mg²⁺ ions with d-electron Co²⁺ ions results in a decrease in Lewis acidity of the binary fluorides.

The binary fluorides, obtained and characterized in this work, can find application to many areas, among other things as catalysts and catalyst supports or as components of lithium-ion batteries.

Conflicts of interest

There are no conflicts of interest to declare.

References

- 1 M. Wojciechowska, M. Zielinski and M. Pietrowski, *J. Fluorine Chem.*, 2003, **120**, 1–11.
- 2 E. Kemnitz, *Catal. Sci. Technol.*, 2015, **5**, 786–806.
- 3 M. Pietrowski, M. Zielinski and M. Wojciechowska, *Chemcatchem*, 2011, **3**, 835–838.



- 4 M. Pietrowski, *Green Chem.*, 2011, **13**, 1633–1635.
- 5 M. Zielinski, M. Pietrowski, A. Kiderys, M. Kot and E. Alwin, *J. Fluorine Chem.*, 2017, **195**, 18–25.
- 6 M. Zielinski, A. Kiderys, M. Pietrowski, I. Tomska-Foralewska and M. Wojciechowska, *Catal. Commun.*, 2016, **76**, 54–57.
- 7 M. Zielinski, M. Pietrowski and M. Wojciechowska, *Chemcatchem*, 2011, **3**, 1653–1658.
- 8 A. Tressaud and K. R. Poeppelmeier, *Photonic and electronic properties of fluoride materials: progress in fluorine science series*, Elsevier, 2016.
- 9 S. Fujihara and K. Tokumo, *J. Fluorine Chem.*, 2009, **130**, 1106–1110.
- 10 S. Sakka, *Handbook of Sol-Gel Science and Technology Processing, Characterization and Applications*, Kluwer Academic Publishers, Boston, Dordrecht, London, 2005.
- 11 P. P. Fedorov, A. A. Luginina, S. V. Kuznetsov and V. V. Osiko, *J. Fluorine Chem.*, 2011, **132**, 1012–1039.
- 12 Y. T. Teng, F. X. Wei and R. Yazami, *J. Alloys Compd.*, 2015, **653**, 434–443.
- 13 Y. T. Teng, S. S. Pramana, J. F. Ding, T. Wu and R. Yazami, *Electrochim. Acta*, 2013, **107**, 301–312.
- 14 Y. Han, H. Li, J. Li, H. Si, W. Zhu and X. Qiu, *ACS Appl. Mater. Interfaces*, 2016, **8**, 32869–32874.
- 15 Y. Lu, Z. Y. Wen, J. Jin, K. Rui and X. W. Wu, *Phys. Chem. Chem. Phys.*, 2014, **16**, 8556–8562.
- 16 H. Groult, S. Neveu, S. Leclerc, A. G. Porras-Gutierrez, C. M. Julien, A. Tressaud, E. Durand, N. Penin and C. Labrugere, *J. Fluorine Chem.*, 2017, **196**, 117–127.
- 17 J. L. Tan, L. Liu, S. P. Guo, H. Hu, Z. C. Yan, Q. Zhou, Z. F. Huang, H. B. Shu, X. K. Yang and X. Y. Wang, *Electrochim. Acta*, 2015, **168**, 225–233.
- 18 X. R. Wang, W. T. Gu, J. T. Lee, N. Nitta, J. Benson, A. Magasinski, M. W. Schauer and G. Yushin, *Small*, 2015, **11**, 5164–5173.
- 19 X. D. Li, R. Ding, W. Shi, Q. L. Xu and E. H. Liu, *Chem.–Eur. J.*, 2017, **23**, 6896–6904.
- 20 D. S. Jacob, L. Bitton, J. Grinblat, I. Felner, Y. Koltypin and A. Gedanken, *Chem. Mater.*, 2006, **18**, 3162–3168.
- 21 A. Saberi, Z. Negahdari, S. Bouazza and M. Willert-Porada, *J. Fluorine Chem.*, 2010, **131**, 1353–1355.
- 22 G. Scholz, and E. Kemnitz, in *Modern Synthesis Processes and Reactivity of Fluorinated Compounds: Progress in Fluorine Science*, ed. H. Groult, F. Leroux, and A. Tressaud, Elsevier, 2017, pp. 609–649.
- 23 E. Kemnitz and J. Noack, *Dalton Trans.*, 2015, **44**, 19411–19431.
- 24 T. Murata, H. Ishizawa, I. Motoyama and A. Tanaka, *Appl. Opt.*, 2006, **45**, 1465–1468.
- 25 A. B. D. Nandiyanto, T. Ogi and K. Okuyama, *ACS Appl. Mater. Interfaces*, 2014, **6**, 4418–4427.
- 26 A. B. D. Nandiyanto, F. Iskandar, T. Ogi and K. Okuyama, *Langmuir*, 2010, **26**, 12260–12266.
- 27 Z. H. Li, Z. Jia, Y. X. Luan and T. C. Mu, *Curr. Opin. Solid State Mater. Sci.*, 2008, **12**, 1–8.
- 28 T. Skapin, G. Tavcar, A. Bencan and Z. Mazej, *J. Fluorine Chem.*, 2009, **130**, 1086–1092.
- 29 B. Ruprecht, M. Wilkening, S. Steuernagel and P. Heitjans, *J. Mater. Chem.*, 2008, **18**, 5412–5416.
- 30 S. Rüdiger, U. Gross and E. Kemnitz, *J. Fluorine Chem.*, 2007, **128**, 353–368.
- 31 J. K. Murthy, U. Gross, S. Rüdiger, E. Unveren and E. Kemnitz, *J. Fluorine Chem.*, 2004, **125**, 937–949.
- 32 J. K. Murthy, U. Gross, S. Rüdiger and E. Kemnitz, *Appl. Catal., A*, 2004, **278**, 133–138.
- 33 S. N. Achary, S. J. Patwe and A. K. Tyagi, *Mater. Res. Bull.*, 2000, **35**, 1167–1169.
- 34 M. Cao, Y. Wang, Y. Qi, C. Guo and C. Hu, *J. Solid State Chem.*, 2004, **177**, 2205–2209.
- 35 J. Haber and M. Wojciechowska, *J. Catal.*, 1988, **110**, 23–36.
- 36 M. Wojciechowska, B. Czajka, M. Pietrowski and M. Zielinski, *Catal. Lett.*, 2000, **66**, 147–153.
- 37 E. Kemnitz, U. Gross, S. Rüdiger and C. S. Shekar, *Angew. Chem., Int. Ed.*, 2003, **42**, 4251–4254.
- 38 E. Kemnitz, G. Scholz and S. Rüdiger, in *Functionalized Inorganic Fluorides: Synthesis, Characterization & Properties of Nanostructured Solids*, ed. A. Tressaud, John Wiley & Sons, 2010, pp. 1–38.
- 39 S. Abbas, Y. Huang, J. Lin, A. Abbas, X. W. Xu, J. Li, S. Wang, X. Jin and C. C. Tang, *RSC Adv.*, 2016, **6**, 29818–29822.
- 40 S. Wutke, A. Vimont, J. C. Lavalley, M. Daturi and E. Kemnitz, *J. Phys. Chem. C*, 2010, **114**, 5113–5120.
- 41 E. Kemnitz, S. Wuttke and S. M. Coman, *Eur. J. Inorg. Chem.*, 2011, **31**, 4773–4794.
- 42 E. Kemnitz, Y. Zhu and B. Adamczyk, *J. Fluorine Chem.*, 2002, **114**, 163–170.
- 43 K. Tanabe, T. Sumiyoshi, K. Shibata, T. Kiyoura and J. Kitagawa, *Bull. Chem. Soc. Jpn.*, 1974, **47**, 1064–1066.
- 44 B. Adamczyk, A. Hess and E. Kemnitz, *J. Mater. Chem.*, 1996, **6**, 1731–1735.
- 45 H. Lee, H. S. Kim, H. Kim, W. S. Jeong and I. Seo, *J. Mol. Catal. A: Chem.*, 1998, **136**, 85–89.
- 46 J. Krishna Murthy, U. Gross, S. Rüdiger, E. Unveren, W. Ünger and E. Kemnitz, *Appl. Catal., A*, 2005, **282**, 85–91.
- 47 H. A. Prescott, Z. J. Li, E. Kemnitz, J. Deutsch and H. Lieske, *J. Mater. Chem.*, 2005, **15**, 4616–4628.
- 48 S. Wuttke, S. M. Coman, G. Scholz, H. Kirmse, A. Vimont, M. Daturi, S. L. M. Schroeder and E. Kemnitz, *Chem.–Eur. J.*, 2008, **14**, 11488–11499.
- 49 S. Celerier and F. Richard, *Catal. Commun.*, 2015, **67**, 26–30.
- 50 Z. W. Fu, C. L. Li, W. Y. Liu, J. Ma, Y. Wang and Q. Z. Qin, *J. Electrochem. Soc.*, 2005, **152**, E50–E55.
- 51 M. J. Armstrong, A. Panneerselvam, C. O'Regan, M. A. Morris and J. D. Holmes, *J. Mater. Chem.*, 2013, **1**, 10667–10676.
- 52 S. B. Ni, J. J. Ma, J. C. Zhang, X. L. Yang and L. L. Zhang, *Mater. Lett.*, 2015, **139**, 138–140.
- 53 Z. Y. Zhang, W. Y. Li, R. J. Zou, W. P. Kang, Y. S. Chui, M. F. Yuen, C. S. Lee and W. J. Zhang, *J. Mater. Chem. A*, 2015, **3**, 6990–6997.
- 54 R. A. Quinlan, Y. C. Lu, D. Kwabi, Y. Shao-Horn and A. N. Mansour, *J. Electrochem. Soc.*, 2016, **163**, A300–A308.
- 55 R. D. Shannon and C. T. Prewitt, *Acta Crystallogr., Sect. B: Struct. Sci.*, 1969, **B 25**, 925–946.



- 56 K. V. K. Rao, S. V. N. Naidu and P. L. N. Setty, *Acta Crystallogr.*, 1962, **15**, 528–530.
- 57 W. H. Baur and A. A. Khan, *Acta Crystallogr., Sect. B: Struct. Sci.*, 1971, **B 27**, 2133–2139.
- 58 J. P. Vidal, G. Vidal-Valat, M. Galtier and K. Kurkisuonio, *Acta Crystallogr., Sect. A: Cryst. Phys., Diff., Theor. Gen. Crystallogr.*, 1981, **37**, 826–837.
- 59 J. W. Stout and S. A. Reed, *J. Am. Chem. Soc.*, 1954, **76**, 5279–5281.
- 60 M. M. R. Costa, J. A. Paixao, M. J. M. Dealmeida and L. C. R. Andrade, *Acta Crystallogr., Sect. B: Struct. Sci.*, 1993, **49**, 591–599.
- 61 H. F. Gong, J. J. Zhu, K. L. Lv, P. Xiao and Y. X. Zhao, *New J. Chem.*, 2015, **39**, 9380–9388.
- 62 Y. H. Zhang, H. F. Xiong, K. Y. Liew and J. L. Li, *J. Mol. Catal. A: Chem.*, 2005, **237**, 172–181.
- 63 L. F. Liotta, G. Di Carlo, G. Pantaleo, A. M. Venezia and G. Deganello, *Appl. Catal., B*, 2006, **66**, 217–227.
- 64 C. W. Tang, C. B. Wang and S. H. Chien, *Thermochim. Acta*, 2008, **473**, 68–73.
- 65 J. Li, G. Z. Lu, G. S. Wu, D. S. Mao, Y. L. Guo, Y. Q. Wanga and G. A. Yun, *Catal. Sci. Technol.*, 2014, **4**, 1268–1275.
- 66 A. Infantes-Molina, J. Mérida-Robles, E. Rodríguez-Castellón, J. L. G. Fierro and A. Jiménez-López, *Appl. Catal., A*, 2008, **341**, 35–42.
- 67 M. Wojciechowska, M. Zielinski, A. Malczewska, W. Przysajko and M. Pietrowski, *Appl. Catal., A*, 2006, **298**, 225–231.
- 68 J. C. Oxley, S. M. Kaushik and N. S. Gilson, *Thermochim. Acta*, 1989, **153**, 269–286.
- 69 J. C. Oxley, J. L. Smith, E. Rogers and M. Yu, *Thermochim. Acta*, 2002, **384**, 23–45.
- 70 K. R. Brower, J. C. Oxley and M. Tewari, *J. Phys. Chem.*, 1989, **93**, 4029–4033.
- 71 M. Thommes, K. Kaneko, A. V. Neimark, J. P. Olivier, F. Rodriguez-Reinoso, J. Rouquerol and K. S. W. Sing, *Pure Appl. Chem.*, 2015, **87**, 1051–1069.
- 72 L. P. Wang, P. D. Han, Z. X. Zhang, C. L. Zhang and B. S. Xu, *Comput. Mater. Sci.*, 2013, **77**, 281–285.
- 73 S. Ghahramani and H. Kangarlau, *J. Nano- Electron. Phys.*, 2013, **5**, 04051.
- 74 K. R. Babu, C. B. Lingam, S. Auluck, S. P. Tewari and G. Vaitheeswaran, *J. Solid State Chem.*, 2011, **184**, 343–350.
- 75 S. J. Splinter, N. S. McIntyre, W. N. Lennard, K. Griffiths and G. Palumbo, *Surf. Sci.*, 1993, **292**, 130–144.
- 76 C. Chen, S. J. Splinter, T. Do and N. S. McIntyre, *Surf. Sci.*, 1997, **382**, L652–L657.
- 77 N. S. McIntyre and C. Chen, *Corros. Sci.*, 1998, **40**, 1697–1709.
- 78 H. B. Yao, Y. Li and A. T. S. Wee, *Appl. Surf. Sci.*, 2000, **158**, 112–119.
- 79 S. Verdier, N. van der Laak, S. Delalande, J. Metson and F. Dalard, *Appl. Surf. Sci.*, 2004, **235**, 513–524.
- 80 V. Fournier, P. Marcus and I. Olefjord, *Surf. Interface Anal.*, 2002, **34**, 494–497.
- 81 P. A. Sermon and R. Badheka, *J. Sol-Gel Sci. Technol.*, 2004, **32**, 149–153.
- 82 M. Santamaria, F. Di Quarto, S. Zanna and P. Marcus, *Electrochim. Acta*, 2007, **53**, 1314–1324.
- 83 S. Verdier, S. Delalande, N. van der Laak, J. Metson and F. Dalard, *Surf. Interface Anal.*, 2005, **37**, 509–516.
- 84 J. L. Booster, J. H. L. Voncken, A. van Sandwijk and M. A. Reuter, *Powder Diff.*, 2002, **17**, 112–118.
- 85 S. Wuttke, S. M. Coman, J. Krohnert, F. C. Jentoft and E. Kemnitz, *Catal. Today*, 2010, **152**, 2–10.
- 86 W. A. Crichton, J. B. Parise, H. Mueller, J. Breger, W. G. Marshall and M. D. Welch, *Mineral. Mag.*, 2012, **76**, 25–36.
- 87 A. Demourgues, N. Penin, D. Dambournet, R. Clarenc, A. Tressaud and E. Durand, *J. Fluorine Chem.*, 2012, **134**, 35–43.
- 88 M. Liu, S. Zanna, H. Ardelean, I. Frateur, P. Schmutz, G. L. Song, A. Atrens and P. Marcus, *Corros. Sci.*, 2009, **51**, 1115–1127.
- 89 N. S. McIntyre and M. G. Cook, *Anal. Chem.*, 1975, **47**, 2208–2213.
- 90 F. Bensebaa, F. Zavaliche, P. L'Ecuyer, R. W. Cochrane and T. Veres, *J. Colloid Interface Sci.*, 2004, **277**, 104–110.
- 91 S. C. Petitto, E. M. Marsh, G. A. Carson and M. A. Langell, *J. Mol. Catal. A: Chem.*, 2008, **281**, 49–58.
- 92 J. Yang, H. W. Liu, W. N. Martens and R. L. Frost, *J. Phys. Chem. C*, 2010, **114**, 111–119.
- 93 J. J. Zhu, K. Kailasam, A. Fischer and A. Thomas, *ACS Catal.*, 2011, **1**, 342–347.
- 94 L. X. Yang and B. Luan, *J. Electrochem. Soc.*, 2005, **152**, C474–C481.
- 95 A. A. Khassin, T. M. Yurieva, V. V. Kaichev, V. I. Bukhtiyarov, A. A. Budneva, E. A. Paukshtis and V. N. Parmon, *J. Mol. Catal. A: Chem.*, 2001, **175**, 189–204.
- 96 Y. C. Lu, A. N. Mansour, N. Yabuuchi and Y. Shao-Horn, *Chem. Mater.*, 2009, **21**, 4408–4424.
- 97 J. S. Girardon, A. S. Lermontov, L. Gengembre, P. A. Chernavskii, A. Griboval-Constant and A. Y. Khodakov, *J. Catal.*, 2005, **230**, 339–352.
- 98 R. D. Shannon, *Acta Crystallogr., Sect. A: Cryst. Phys., Diff., Theor. Gen. Crystallogr.*, 1976, **32**, 751–767.

